Electronic Supplementary Material (ESI) for Physical Chemistry Chemical Physics.

Exploration of the phase diagram of liquid water in the low-temperature metastable region using synthetic fluid inclusions

Supplementary Material

Chen Qiu[a], Yves Krüger[a,1], Max Wilke[b,2], Dominik Marti[c], Jaroslav Rička[a], and Martin Frenz[a *]

[a]Institute of Applied Physics, University of Bern, Sidlerstrasse 5, 3012 Bern, Switzerland
[b]GeoForschungsZentrum Potsdam, Telegrafenberg, 14473 Potsdam, Germany
[c]Department of Photonics Engineering, Technical University of Denmark, Frederiksborgvej 399, Himmelev, 4000, Roskilde, Denmark

S-2.1. Synthetic fluid inclusions

Synthetic fluid inclusions were produced according to the principles described by Sterner and Bodnar[1] and Bodnar and Sterner.[2] We used natural inclusion-free quartz crystals that were cut in prisms (4.5 mm ×4.5 mm×10 mm) perpendicular to the crystal *c*-axis. The prisms were cleaned following the procedure described by Lin and Bodnar.[3] After cleaning, the prisms were heated to 370 °C in a muffle furnace and then immediately quenched in cold deionized water, inducing numerous cracks in the quartz prisms. After quenching, the pre-fractured prisms were dried at 120 °C.

The capsules used for the hydrothermal fluid inclusion syntheses were prepared from 60 mm long gold tubes (purity grade 99.99%) with 6 mm outer diameter and 0.25 mm wall thickness. The gold tubes were annealed at 800 °C for one hour and subsequently welded at one end. After welding, the empty, open capsule was weighted. A pre-fractured quartz prism was then loaded and its mass was determined by differential weighing. Subsequently, the capsule was completely filled with deionized (air-saturated) water and sealed by squeezing the top 15 mm using a flat-nose pliers. In doing so, the water in the top part was pressed out, making sure that no excess air remains in the capsule. The sealed capsule was then weighted again to determine the amount of water, and finally, the squeezed upper end of the capsule was welded. Later on, during hydrothermal syntheses the water volume expands by up to 9% resulting in fluid overpressure in the capsule and slight ballooning of the squeezed upper capsule part. 12 capsules were prepared for this study with water amounts between 0.45 g and 0.53 g and water/quartz mass ratios between 1.5 and 2.5. Note that neither quartz powder nor silica gel was used to enhance crack healing during the hydrothermal synthesis. Pure water inclusions were produced by hydrothermal synthesis in an internally heated pressure vessel (IHPV) using argon as pressure medium. Synthesis conditions were between 420 °C and 520 °C at pressures ranging from 710 MPa to 860 MPa. Run durations were between 46 and 96 hours. During the hydrothermal experiments, the cracks in the prisms healed by dissolution, transport and re-precipitation of quartz, resulting in a large number of isolated fluid inclusions. The density of the water

[1] present address: Institute of Environmental Physics, University of Heidelberg, Im Neuenheimer Feld 229, 69102 Heidelberg, Germany
[2] present address: Institute of Earth and Environmental Sciences, University of Potsdam, Karl-Liebknecht-Str. 24-25, 14476 Potsdam-Golm, Germany

encapsulated in these fluid inclusions depends on the pressure–temperature (p–T) conditions of the hydrothermal synthesis. For the present study we produced synthetic fluid inclusions covering a range of water densities between 996 kg/m^3 and 919 kg/m^3. Although the aforementioned experiment was designed to get specific density values for the inclusions under given p–T conditions, we have noticed that the stability and the accuracy of the pre-set p–T conditions were insufficient for reliable density calculations and thus, the exact densities of the inclusions had to be determined ex-post from T_h measurements.

In the hydrothermal experiments, the pre-set p–T conditions were obtained first by increasing the pressure to a value slightly above the desired value, in order to check the tightness of the pressure vessel. Then, the temperature was increased to the set value and the pressure was adjusted to the final run conditions. Slight decreases of the pressure during the hydrothermal syntheses were common and were automatically corrected by pumping the system to the set value when pressure dropped by 30 MPa. To terminate the runs, temperature and pressure were decreased stepwise along a quasi-isochoric p–T path to avoid high differential stress in the fluid inclusions. Once the hydrothermal runs were completed, the capsules were cleaned and weighted to check for potential water loss. Afterwards, the capsules were punctured to evaporate the water at 100 °C, and then re-weighted to verify the previously determined water amounts. Note that the small amount of water trapped in the quartz prisms can be ignored.

The quartz prisms were then removed from the gold capsules and cut perpendicular to the long axis into 400 µm thick slices using a low-speed rotary saw (Buehler Isomet) equipped with a 0.3 mm sawing blade. The slices were gound and polished on both sides to a final thickness of 250 µm to 300 µm. The quartz c-axis is parallel to the polished sample surfaces. The shapes of the synthesized fluid inclusions were typically irregular and flat or slightly elongate without negative crystal faces and inclusion sizes are typically below 500 µm^3. In most of the samples, the inclusions were in a monophase liquid state at room temperature and did not show spontaneous bubble nucleation upon further cooling.

S-2.2. Experimental setup

The experimental setup shown in detail in Fig. S-1 is built around an upright microscope (Olympus BX51) and consists of: (i) a heating/cooling stage, (ii) a femtosecond laser system providing amplified ultrashort laser pulses, and (iii) a Raman spectrometer.

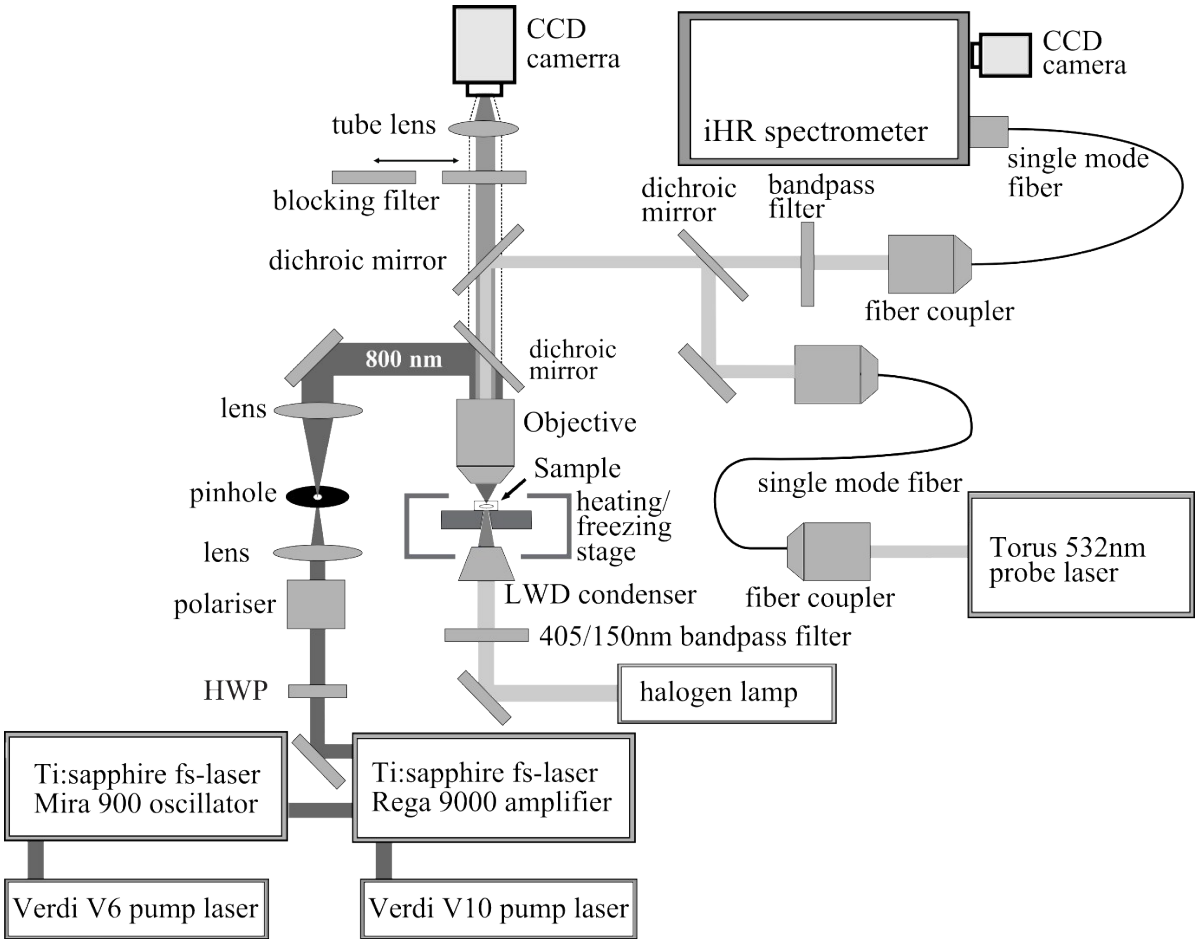

Fig S-1: Schematic representation of the experimental setup used for this study. See text for details.

i) The heating/cooling stage (Linkam THMSG 600) is mounted on the microscope and allows for microthermometric measurements in the temperature range between −180 °C and 600 °C. For visual observations of the inclusions in transmitted light, the microscope is equipped with a 100 W halogen light source, a heat-absorbing filter (KG5, Schott) mounted in the illumination filter block (not shown), a long working distance (LWD) condenser (Linkam) illuminating the sample with a numerical aperture (N.A.) of ~0.4 and, an LWD objective (Olympus LCPLFLN 50×/0.7 LCD) featuring a correction ring for cover glass thickness. The working distance of the objective is between 3.0 and 2.2 mm depending on the thickness of the cover glass. Due to the relatively small working distance of this objective we had to slightly modify the design of the standard lid that seals the sample chamber of the stage. Additionally, the microscope is equipped with a high sensitivity CCD camera (pco.1600) providing real time images of the sample.

ii) A femtosecond (*f-s*) laser system is used to stimulate vapour bubble nucleation in the metastable liquid state of the inclusions by means of single ultrashort laser pulses.[4] The laser system consists of a Ti:sapphire femtosecond oscillator (Coherent Mira 900) and an regenerative amplifier (Coherent RegA 9000). The

oscillator is pumped with a Coherent Verdi V6. The RegA is seeded by the oscillator and pumped with a Coherent Verdi V10. The RegA provides pulse repetition rates of up to 250 kHz, but for our specific application, we use the system in single-pulse mode, triggering single ultrashort laser pulses at the push of a button. The energy of the amplified laser pulse is around 4 µJ at pulse durations in the range of 200 fs (1 fs = 10^{-15} s).

The laser light emitted from the RegA has a central wavelength of 800 nm and, thus, optical components with near infrared (NIR) coatings were used for the setup. From the RegA, the laser beam is guided through a half wave plate (HWP) and a Glan-laser polariser to adjust the laser pulse energy. This is done by rotating the HWP and thus the polarisation direction of the laser beam relative to the polarizer. The beam then passes through a spatial filter and a 2× beam expander consisting of a 100 mm focusing lens, a 50 µm pinhole and a 200 mm collimation lens to enhance the beam quality and to achieve a beam diameter that optimally fills the objective back aperture. The collimated laser beam is then coupled into the microscope through a UD-P dual port adapter (Olympus) equipped with a switchable dichroic mirror (XF 2033, Omega Optical) and focused on the sample through the microscope objective.

When operated in single-pulse mode, the RegA is not pulsing between the single shots and a small fraction of the Mira seed beam is leaking through and can be used for laser alignment. The position of the laser beam focused on the sample can be imaged on the CCD camera. A BG38 bandpass filter (Schott) in a switchable mount is placed in front of the CCD camera to reduce the intensity of the Mira leak beam backscattered from the sample surface.

The experimental setup allows us to stimulate vapour bubble nucleation in selected fluid inclusions at different temperatures and under microscopic observation. Subsequent microthermometric measurements can be performed without moving the sample.

iii) Confocal Raman spectroscopy is used to identify the ice phase in the inclusions in order to determine ice nucleation temperatures. In pure water inclusions the phase transition is not visible from microscopic observations unless a vapour bubble is present that becomes strongly compressed upon ice nucleation. The fiber-coupled Raman setup consists of a 500 mW diode-pumped solid-state single mode linearly polarized laser at 532 nm wavelength with 1 MHz bandwidth, (Torus, Laser Quantum) two dichroic mirrors, a spectrometer (Horiba iHR550M CORE 3) and a back-illuminated CCD camera (Horiba SYNAPSE BIVS).

The probe laser is coupled into a single-mode fiber that serves as a spatial filter. After coupling out of the fiber, the laser beam is directed through a 3× beam expander to achieve an optimum beam diameter. The collimated laser beam is then reflected at a dichroic mirror with a steep edge at 532 nm designed for Raman spectroscopy (Semrock LPD02-532RU) and coupled into the microscope through a second UD-P dual port adapter (Olympus) equipped with a switchable dichroic mirror (Semrock FF740-Di01). Finally, the

excitation beam (60 mW) is focused into the inclusions through the microscope objective that also collects the light that is back-scattered from the sample, i.e., the Raman and Rayleigh scattering. The FF740 dichroic mirror reflects more than 95% of the back-scattered light in the wavelength range between 480 nm and 725 nm and directs it to the 532 nm dichroic mirror. While the Stokes-shifted Raman scattering passes though, the major fraction of the Rayleigh scattering (532 nm) and the anti-Stokes Raman scattering are reflected at the dichroic mirror and thus do not reach the spectrometer. An additional 532 nm long-pass filter (Semrock LP03-532RU) is used to further reduce the intensity of the Rayleigh scattering before the residual light is coupled into a single-mode fiber and guided into the spectrometer to measure the Raman spectra of liquid water and ice.

The FF740 dichroic mirror features an average transmission of 25% in the 380 nm to 460 nm spectral range, which allows us to observe the sample during the Raman measurements. A band-pass filter (Semrock FF01-405/150) selects the required wavelength range from the halogen light source to illuminate the sample from below. In addition, a small fraction of the back-scattered 532 nm light leaks through the dichroic mirror and can be detected with the pco.1600 CCD camera mounted on the microscope. A switchable 532 nm laser rejection filter (Horiba, XB11) placed in front of the camera is used to further reduce the intensity of the Rayleigh back-scattered light.

The Raman setup outlined above allows us to measure Raman spectra at different temperatures under simultaneous observation of the focus position of the excitation beam relative to the fluid inclusion.

S-2.4.2. Effect of surface tension

The surface tension at the liquid–gas interface of the vapour bubble works towards a minimisation of the bubble surface and causes a pressure difference Δp between the liquid and the vapour phase, which is described by the Young-Laplace equation:

$$\Delta p = \frac{2\sigma(T)}{r(T)}$$

Here $\sigma(T)$ denotes the surface tension as a function of temperature and $r(T)$ is the radius of the liquid surface at a given temperature. We note that the radius of the liquid surface, in the case of a vapour bubble, is negative and thus, Δp becomes negative as well. Numerical values of $\sigma(T)$ were derived from IAPWS.[5] For calculations of the retrograde homogenisation temperature $T_{hr\infty}$, we had to extrapolate the polynomial function below 0 °C.

Fig. S-2 schematically illustrates the pressure difference Δp between the liquid (p_L) and the vapour phase (p_V) and the resulting effect on prograde and retrograde liquid–vapour homogenisation T_{hobs} and T_{hrobs}, respectively. The model of Marti et al.[6] revealed that the two-phase liquid-vapour system passes from a stable into metastable state at the so-called bubble binodal (T_{bin}) and, finally becomes mechanically unstable at the so-called bubble spinodal (T_{sp}). The homogenisation of the system into a stable liquid state occurs between T_{bin} and T_{sp} due to the collapse of the vapour bubble from a non-zero radius. We therefore need to emphasise that the observed homogenisation temperatures T_{hobs} and T_{hrobs}, are not clearly defined. For the calculation of $T_{h\infty}$ we assumed that the vapour bubble collapses at the bubble spinodal T_{sp}, which implicates a potential underestimation by up to 0.25 °C for the inclusions analysed in this study. For retrograde homogenisation, on the other hand, the same assumption results in a potential overestimation of $T_{hr\infty}$ by up to 0.16 °C.

S-2.4.3. Deviation from the isochoric system

Fig. S-3 illustrates the difference between a true isochore and a pseudo-isochoric curve that was corrected for the temperature-dependent volume changes of the quartz host. The two *p*–*T* curves intersect at the prograde homogenisation temperature $T_{h\infty}$ that denotes the reference temperature at which the isochoric and the quartz-confined system exhibit the same bulk density. At temperatures below $T_{h\infty}$ the volume change of the quartz host results in a decrease of the inclusion volume and thus in an increase of the water density. As a consequence, the pseudo-isochore runs at less negative pressure and the retrograde homogenisation $T_{hr\infty}$ is shifted towards a higher temperature compared to the isochoric system. Fig. S-3 also shows that the pressure minimum of the isochore is defined by the *TMD* line that intersects the liquid–vapour curve at 4 °C. The pressure minima of the pseudo-isochore curves, in contrast, are shifted to higher temperatures and form a Temperature of Minimum Pressure (*TMP*) line that, in the case of a quartz host,

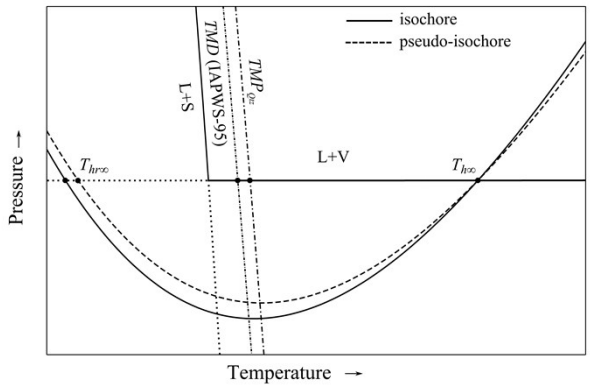

Fig. S-3: Schematic *p*–*T* phase diagram illustrating the non-isochoric behaviour of fluid inclusions due to the temperature-dependent volume change of the quartz host. Solid curve indicates a liquid-isochore, while the dashed line represents the corresponding pseudo-isochore curve. Dash-dotted lines represent the Temperature of Maximum Density (*TMD*) line and the Temperature of Minimum Pressure (TMP_{Qtz}) line in the quartz confined system, respectively. See text for details.

intersects the liquid-vapour curve at 6.15 °C.[7] This means that the temperature at which $T_{h\infty}$ and $T_{hr\infty}$ become equal is shifted from 4 °C in an isochoric system to 6.15 °C in a quartz confined system (see also Fig. 10 in the main article).

A correction for the temperature-dependent volume change of the quartz host was implemented in the numerical iteration routine that calculates of the bulk density $\varrho bulk$ and the volume V of the inclusions at $T_{h\infty}$.

S-3.2. Ice nucleation data

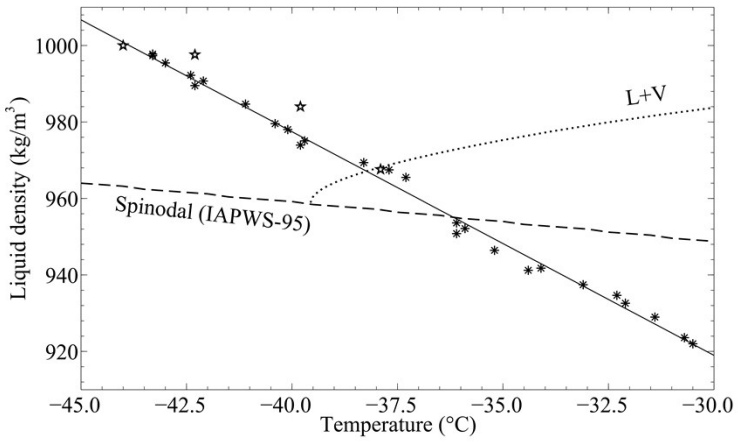

Fig. S-4: Detail of the $\varrho - T$ diagram of water displaying ice nucleation data (L→S) derived from this study (eight spoked asterisk) and from Kanno and Miyata[8] (stars).

Solid line: linear fit to our data. Dotted line: liquid-vapour equilibrium curve (L+V) extrapolated from IAPWS-95. Dashed line: liquid-spinodal (IAPWS-95).

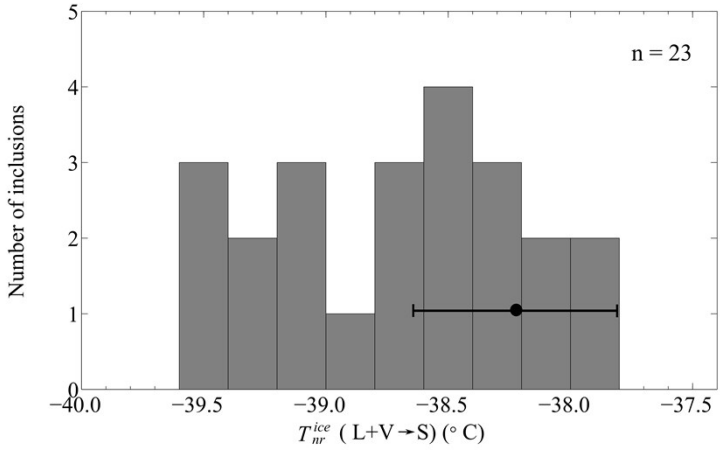

Fig. S-5: Distribution of values measured at saturation pressure (L+V→S). The diagram displays only the lowest value of each inclusion analysed. Black dot with error bar indicates the intersection of the ice nucleation curve (L→S) with the liquid-vapour (L+V) curve (see Fig. S-4).

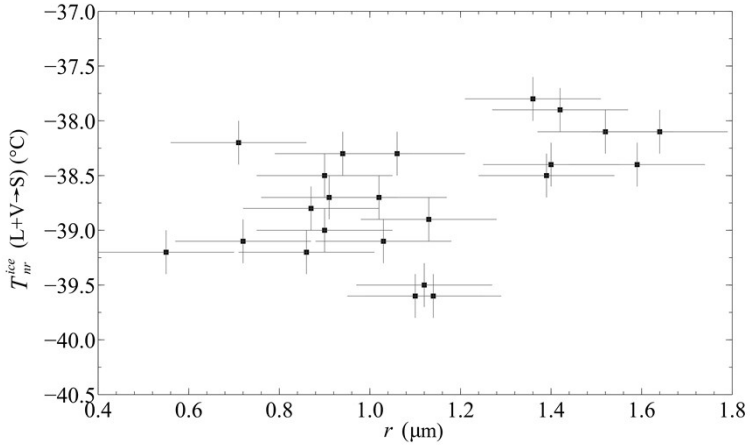

Fig. S-6: Minimun values (L+V→S) plotted against the radius of the vapour bubble at ice nucleation. The diagram indicates a weak correlation of with bubble size, i.e., with the volume of the inclusions.

S-4.1. Evaluation of saturation liquid densities in the supercooled region

In Fig. S-7 we plotted the deviation of the retrograde homogenisation $T_{hr\infty}$ (black dots with error bars) from the reference curve (zero line). In principle, we may assume that the $T_{h\infty}$ values of prograde homogenisation are more accurate than those of $T_{hr\infty}$ because their calculations do not rely on uncertain extrapolations into the supercooled region. Considering $T_{h\infty}$ as 'true' values, the errors associated with the determination of $T_{h\infty}$ manifest as uncertainty of the reference line (grey bars). The $T_{hr\infty}$ values display random scatter and match the reference line within errors.

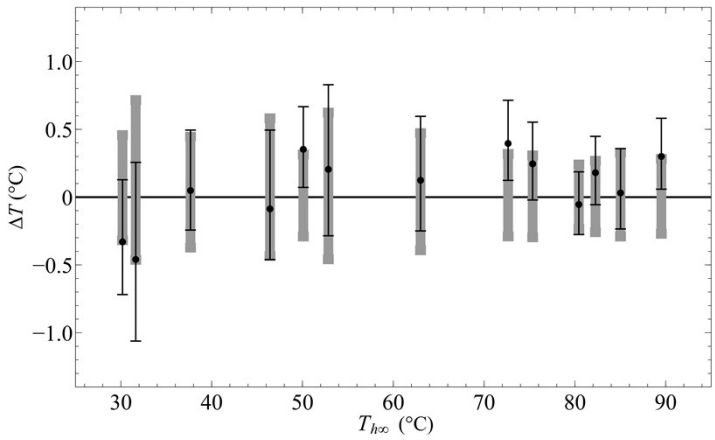

Fig. S-7: Deviation of retrograde homogenisation temperatures $T_{hr\infty}$ from the reference curve (solid line) shown in Fig. 10 of the main article. Zero line = reference curve. Dots with error bars: $T_{hr\infty}$. Grey bars: error of $T_{h\infty}$.

1 S. M. Sterner and R. J. Bodnar, *Geochim. Cosmochim. Acta*, 1984, **48**, 2659–2668.

2 R. J. Bodnar and S. M. Sterner, in *Hydrothermal experimental techniques*, eds. G. C. Ulmer and H. L. Barnes, J. Wiley & Sons, 1987, pp. 423–457.

3 F. Lin and R. J. Bodnar, *Geochim. Cosmochim. Acta*, 2010, **74**, 3260–3273.

4 Y. Krüger, P. Stoller, J. Rička and M. Frenz, *Eur. J. Mineral.*, 2007, **19**, 693–706.

5 IAPWS, *IAPWS Revised Release on Surface Tension of Ordinary Water Substance*, Moscow, Russia, 2014.

6 D. Marti, Y. Krüger, D. Fleitmann, M. Frenz and J. Rička, *Fluid Phase Equilib.*, 2012, **314**, 13–21.

7 D. Marti, Y. Krüger and M. Frenz, in *ECROFI*, Granada (Spain), 2009, pp. 4–5.

8 H. Kanno and K. Miyata, *Chem. Phys. Lett.*, 2006, **422**, 507–512.